Supporting Information

Deciphering Structure Evolution of Adsorbed •OH Species on Zr-oxo Nodes of UiO-66 to Modulate Methane Hydroxylation

Ling-Chan Tian,[a]† Geqian Fang,[b,c]† Yun Zhou,[a] Wenjun Yu,[b,c] Lin Li,[b] Jin-Nian Hu,[a] Hai-Yan Wang,[a] Jin-Xia Liang,*[a] Chun Zhu,*[a] Xiaodong Wang[b] and Jian Lin*[b]

[a] School of Chemistry and Chemical Engineering, Guizhou University, Guiyang, 550025, China.

[b] CAS Key Laboratory of Science and Technology on Applied Catalysis, Dalian Institute of Chemical Physics, Chinese Academy of Sciences, Dalian 116023, P. R. China.

[c] University of Chinese Academy of Sciences, Beijing 100049, P. R. China.

[†] These authors contributed equally to this work.

*Corresponding authors: liangjx2009@163.com; czhu2014@163.com; jianlin@dicp.ac.cn.

1. The reaction rate constant and free energy correlation

The reaction rate constant of CH_4 on different catalysts is calculated by the Eyring-Polanyi equation based on the transition state theory (TST), which can be written as an equation (1):

$$k^{TST} = \sigma \frac{k_B T}{h} \left(\frac{RT}{P_0}\right)^{\Delta n} e^{-\Delta G^{0,\neq}/(k_B T)} \tag{1}$$

where: σ is the transmission coefficient;

k_B is Boltzmann's constant;

T is the absolute temperature;

h is the Planck's constant;

R is the gas constant;

P0 is the standard atmospheric pressure;

And $-\Delta G^{0,\neq}$ is the free energy of activation, where:

$$-G^{0,\neq}(T) = \Delta G^{0}_{TS}(T) - \Delta G^{0}_{Reactant}(T) \tag{2}$$

We first calculate the free energy of activation. The vibrational partition function is written as Eq. (3):

$$q_{vib} = \prod_i \frac{1}{1 - e^{-\frac{\varepsilon i}{k_B T}}} \tag{3}$$

Where, εi is the vibrational energies.

The internal energy is written as:

$$U_{vib} = \Sigma_i \frac{\varepsilon i}{e^{\frac{\varepsilon i}{k_B T}} - 1} \tag{4}$$

And the entropy, S, is calculated via:

$$S_{vib} = k_B \Sigma_i \frac{\varepsilon i}{k_B T\left(e^{\frac{\varepsilon i}{k_B T}} - 1\right)} - In\left(1 - e^{-\frac{\varepsilon i}{k_B T}}\right) \tag{5}$$

Since the zero-point vibrational energy (ZPVE) has already been considered in the reaction energy profiles, the thermal correction to $\Delta G(T)$ in the present work at 298.15 K and P = 1atm is defined as Eq. (6):

$$G_{corr}(298.15\ K) = U_{vib}(298.15\ K) + 298.15 * S_{vib}(298.15\ K) \tag{6}$$

By using the VASPkit processing tool [1], several activation free energies $-\Delta G^{0,\neq}$ are calculated, and then the related reaction rate constants are calculated.

2. The electron density difference

The differential electron densities can be used to explain the change of the charge densities during the chemical reaction or when the molecule binds to the surface. And the changes of electron distribution during the formation of chemical bonds are given by formula (7):

$$\Delta\rho = \rho_{AB} - (\rho_A + \rho_B) \tag{7}$$

Where ρ_{AB} is the electron density of the total system, and ρ_A and ρ_B are the undisturbed electron densities of adsorbed substances and substrates, respectively.

3. Catalytic performance evaluation

Catalyst testing for the oxidation of methane with H_2O_2 was carried out in a 50 mL stainless-steel autoclave containing a Teflon liner vessel with a total volume of 38 mL. The vessel was charged with 10 mg catalyst, 20 mL dilute H_2O_2 solution (0.25 M). After sealing, the reactor was flushed with 5 bar methane for 5 times to remove the contaminant gasses and then charged to 3 MPa methane. The autoclave was heated to 50 °C with vigorous stirring at 1200 rpm. The reactions were carried out for 30 min, after which the vessel was cooled in ice-water bath to minimize the volatility of products. The resultant solution after filtration was analyzed by Nuclear magnetic resonance (NMR) spectroscopy, which were acquired on Bruker AVANCE III HD 700 MHz spectrometer equipped with pulsed field gradient probes. The amount of CH_3OOH, $HOCH_2OOH$ was obtained with the same equation of CH_3OH. Usually, 0.6 mL collected filtrate and 0.1 mL of D_2O (with 0.02 wt% versus 3-(trimethylsilyl)-1-propanesulfonic acid sodium salt (DSS) as internal standard) were mixed in an NMR tube for analysis. During NMR measurements, a solvent suppression program was run in order to minimize the signal originated from H_2O. The gaseous products were analyzed by Agilent 7890B gas chromatograph (GC) system with a thermal conductivity detector (TCD) and flame ionization detector (FID) and a nickel (Ni) catalyst convertor that could quantitatively transform the carbon oxides into methane. This system contains Porapak Q columns for the separation of gaseous

products. The oxygenates selectivity (%), oxygenates yields (μmol g_{cat}^{-1} h^{-1}) were calculated by the following equations (8-9):

$$\text{Oxygenates selectivity} = \frac{n_{(\text{oxygenates products})}}{n_{(\text{total products})}} \times 100\% \tag{8}$$

$$\text{Oxygenates yields} = \frac{n_{(\text{oxygenates products})}}{m_{cat.} \times t} \tag{9}$$

4. Catalyst characterizations

X-ray diffraction (XRD) data were collected on a X'pert Pro-1 (PANalytical) diffractometer with a copper anode (Cu *K*α, λ = 1.5432 Å), operating at 40 kV and 40 mA with a scanning angel (2-theta) from 5º to 50º.

The morphology of the MOFs was characterized using a JSM-7800F Scanning electron microscope (SEM) with an accelerating voltage of 30.0 kV.

Electron paramagnetic resonance (EPR) spectroscopic measurements were obtained at room temperature using a Bruker A200 EPR spectrometer operated at X-band frequency with using 5,5-dimethyl-1-pyrroline N-Oxide (DMPO) as spin trapping agent for free radical. The EPR characterization details in our manuscript are as follows: 0.1 mL radical capture agent of DMPO aqueous solution (28 mg mL^{-1}) was pre-added into a 2 mL brown flask. The reaction solution (0.1 mL) before methane addition and after methane oxidation at 50 °C for 30 min was collected into the brown flask from the vessel and stirred for 1 min to fully capture the free radical species. Then, the mixture was filtered and frozen by liquid N_2. These samples were thawed

subsequently for the EPR measurements. The parameters for EPR measurements were as follows: microwave frequency of 9.3 GZ, microwave power of 10 mW, and modulation frequency of 100 kHz.

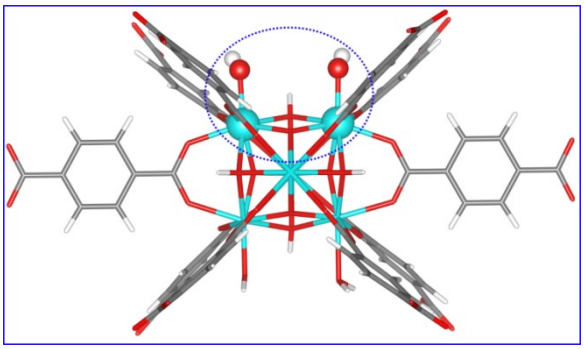

Fig. S1 Missing-ligand defect of UiO-66-H with two Zr_{oxo}-(•OH/•OH) active centers. Color scheme: Blue (Zr), red (O), gray (C), white (H).

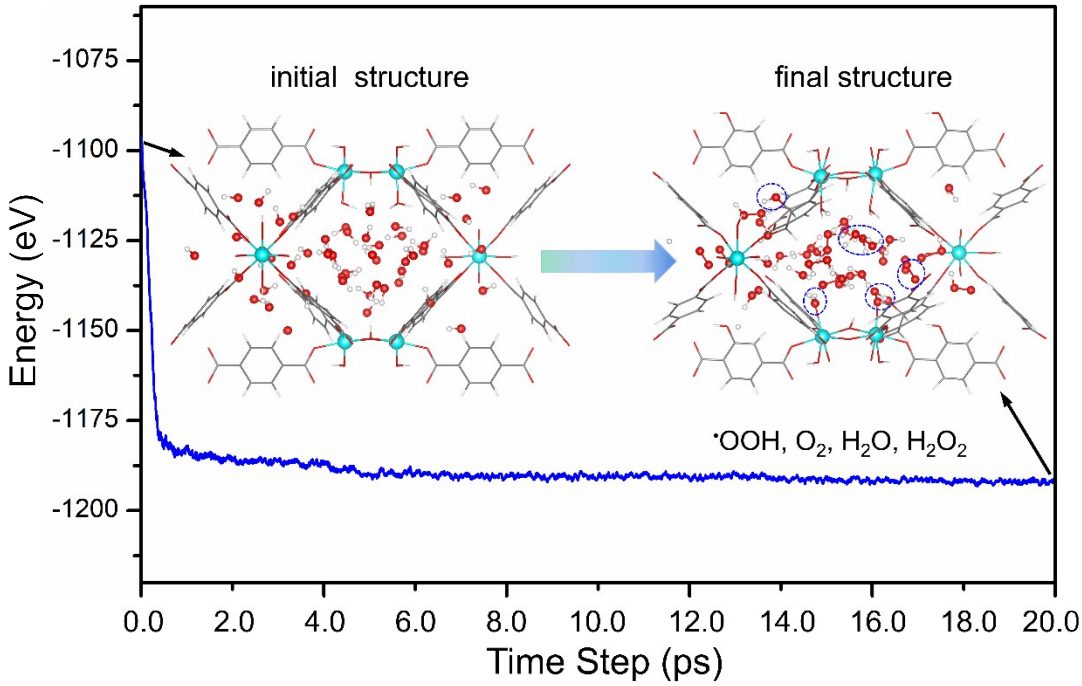

Fig. S2 The total energy and the initial and the final snapshots of AIMD simulation on the structure evolution of Zr-oxo nodes with high •OH concentration at 25°C.

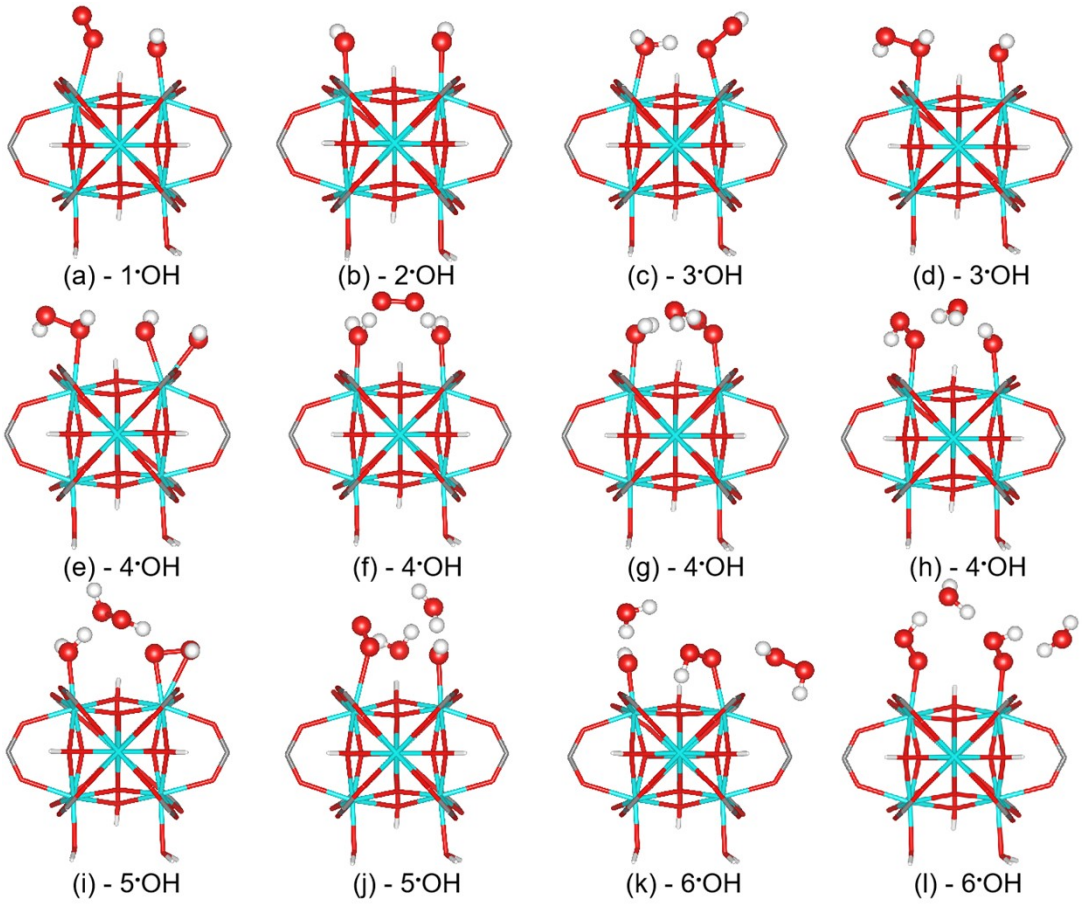

Fig. S3 In UiO-66-H, the configurations of different active sites corresponding to the increase of •OH concentration, (a, b) the geometric structure of 1•OH and 2•OH, respectively, (c, d) the geometric structures of 3•OH, (e–h) corresponding to the geometric structure of 4•OH, (i, j) the geometric structures of 5•OH, and (k, l) the geometric structures of 6•OH. Color scheme: C (gray), H (white), O (red), and Zr (light blue).

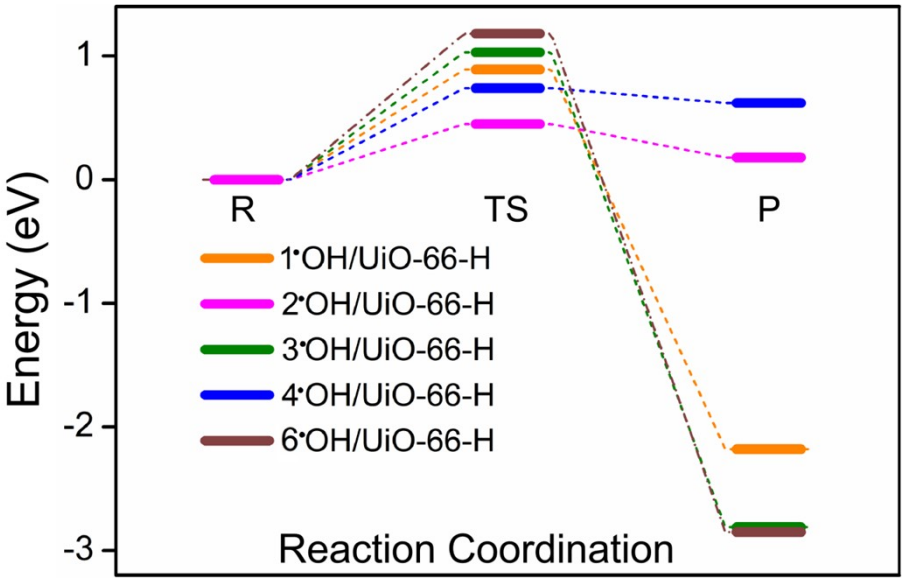

Fig. S4 The calculated energy barrier of $^{\bullet}CH_3$ generated on the Zr-oxo nodes adsorbed by $^{\bullet}OH$ or $^{\bullet}OOH$ species over UiO-66-H catalysts with increasing $^{\bullet}OH$ amount.

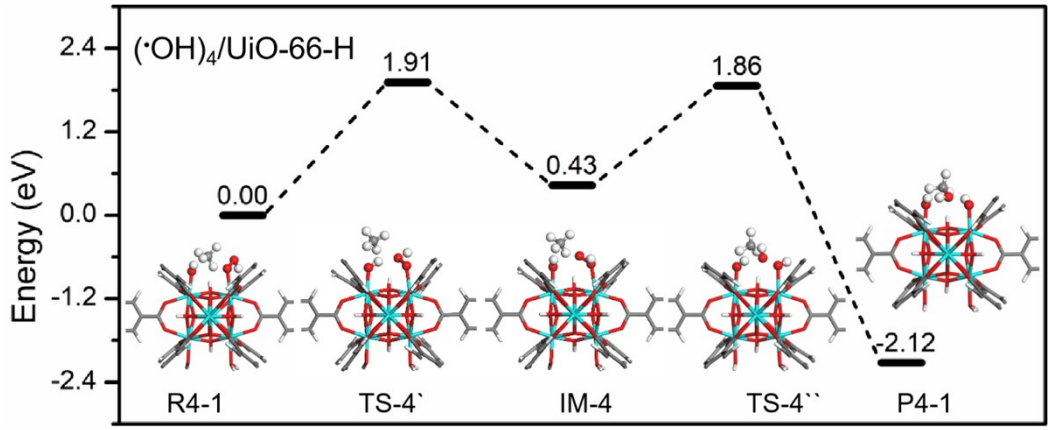

Fig. S5 The predicted profile of reaction pathway for the DSOM reaction on Zr- •OOH active site of Zr-(•OOH/•OH) in R4.

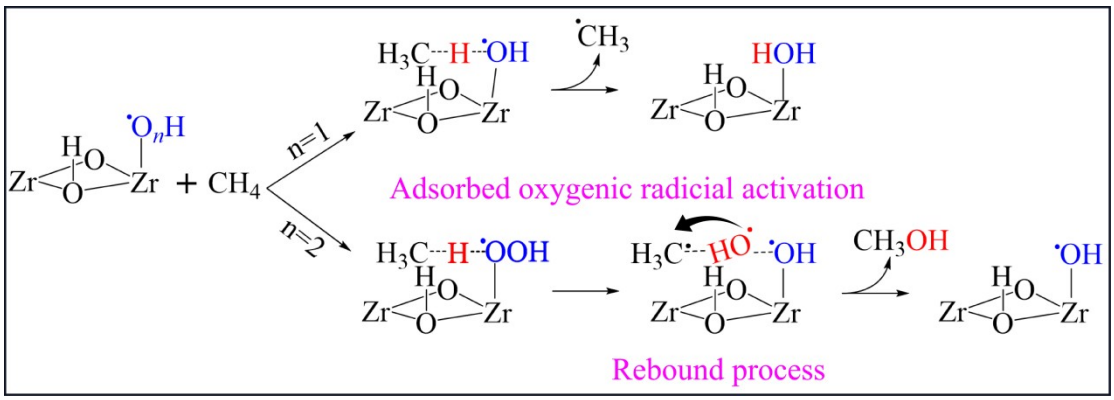

Fig. S6 Proposed H-atom abstraction/radical methane activation mechanism on Zr-oxo nodes of UiO-66-H catalyst.

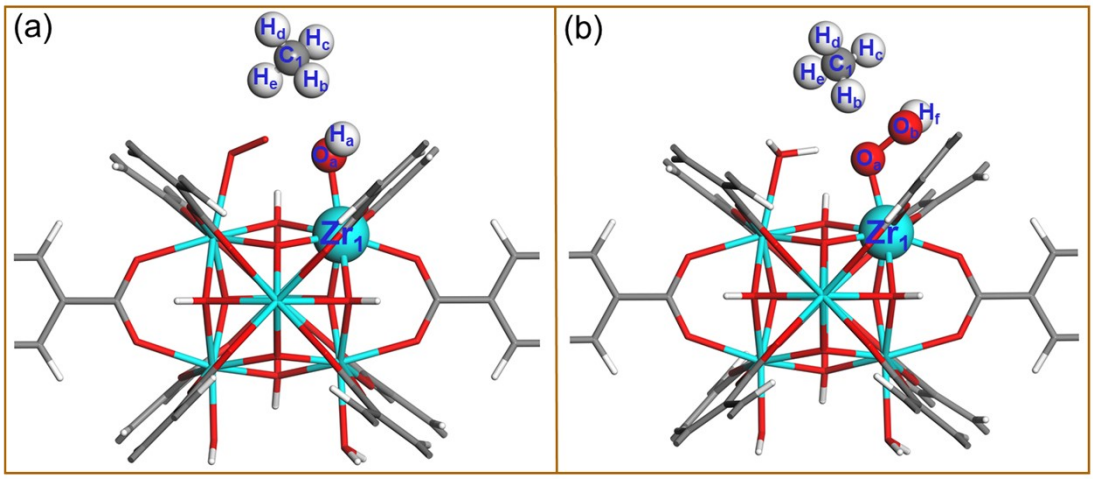

Fig. S7 The atomic number of CH_4 activation catalyzed by the Zr-oxo nodes, (a) and (b) the activation of CH_4 on the Zr-oxo nodes adsorbed with $^{\bullet}OH$ and $^{\bullet}OOH$ species, respectively. Color scheme: C (gray), H (white), O (red), and Zr (light blue). $^{\bullet}O_aH_a$ or $^{\bullet}O_aO_bH_f$ are adsorbed on Zr atom. H_b is the atom transferred from CH_4 to $^{\bullet}O_aH_a$* or $^{\bullet}O_aO_bH_f$*.

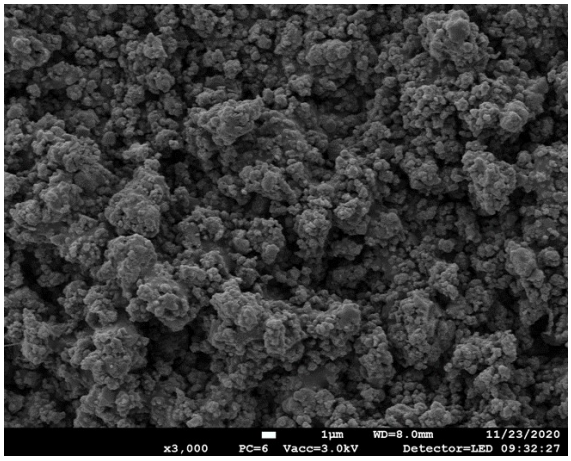

Fig. S8 Representative SEM image of UiO-66-H.

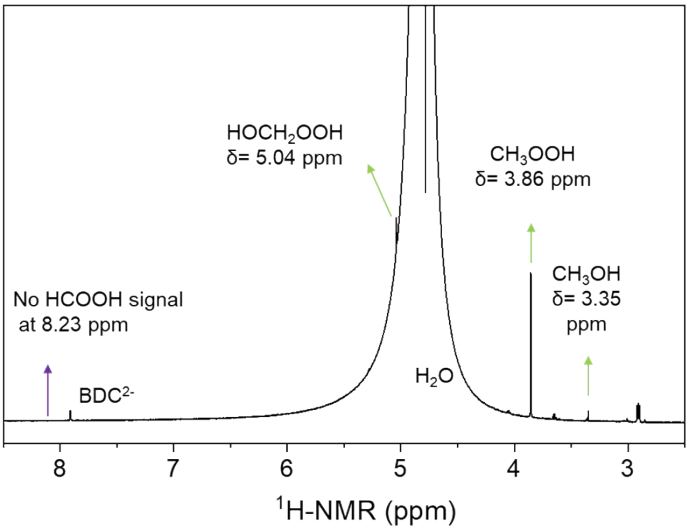

Fig. S9 The ^{1}H-NMR spectrum for the oxygenates produced on UiO-66-H.

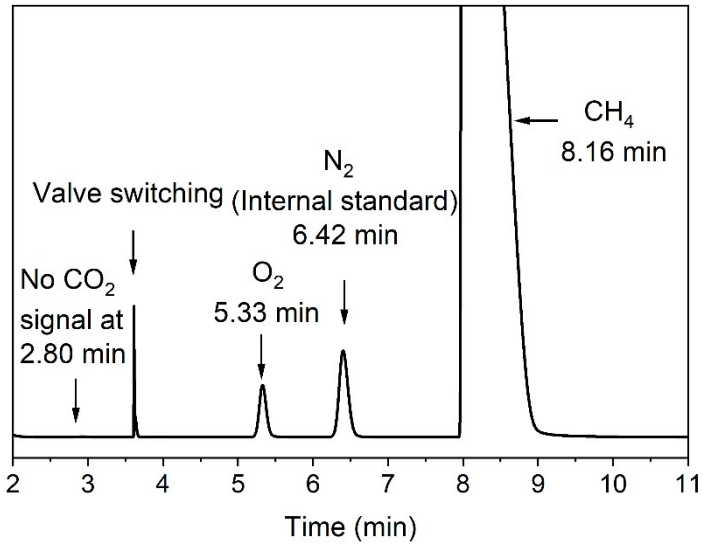

Fig. S10 The TCD spectra for gaseous products over UiO-66-H.

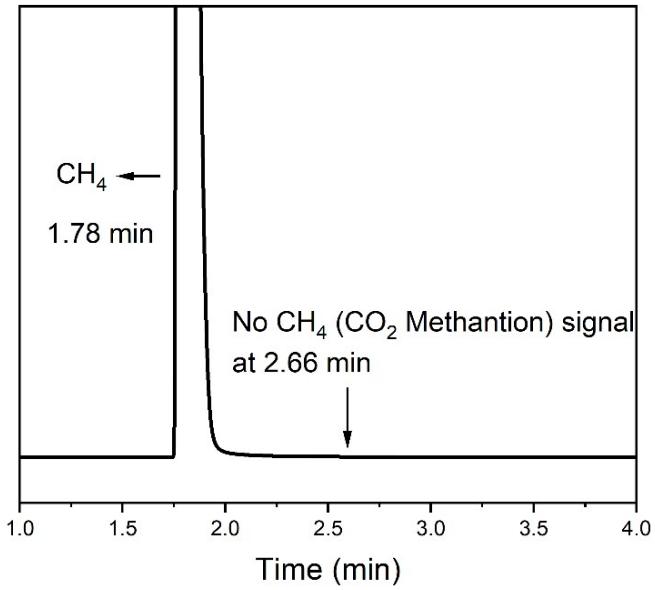

Fig. S11 The FID spectra for gaseous products over UiO-66-H.

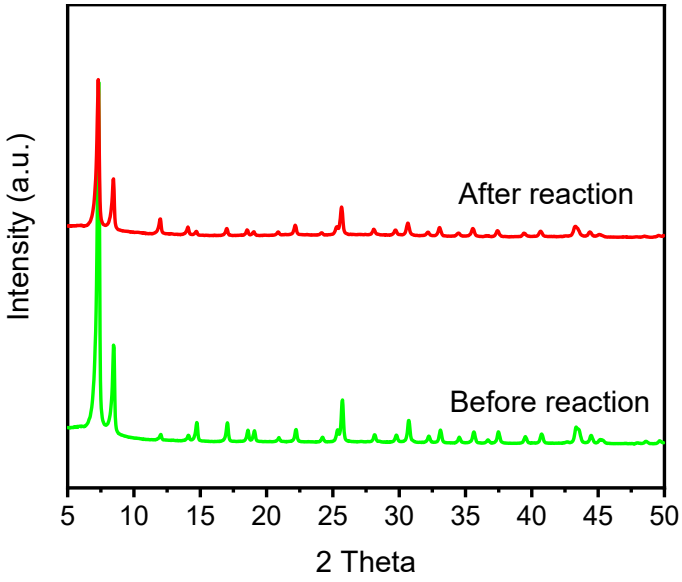

Fig. S12 XRD patterns of UiO-66-H catalysts before and after reaction.

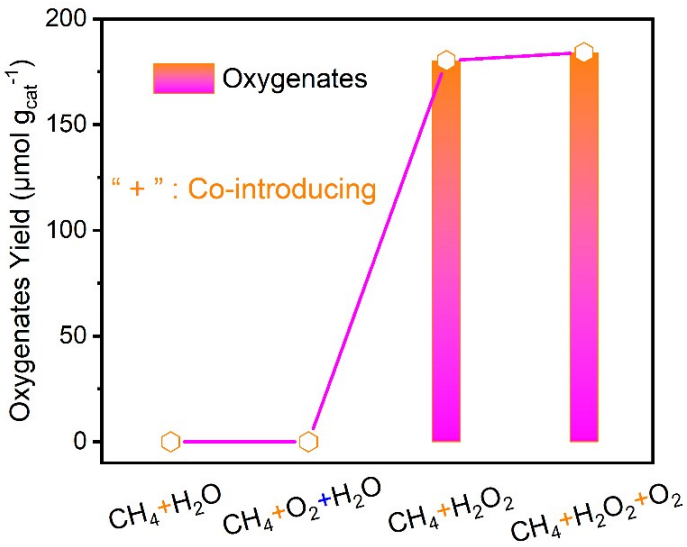

Fig. S13 The controlled experiments by using different reactants (O_2, H_2O_2 and CH_4).

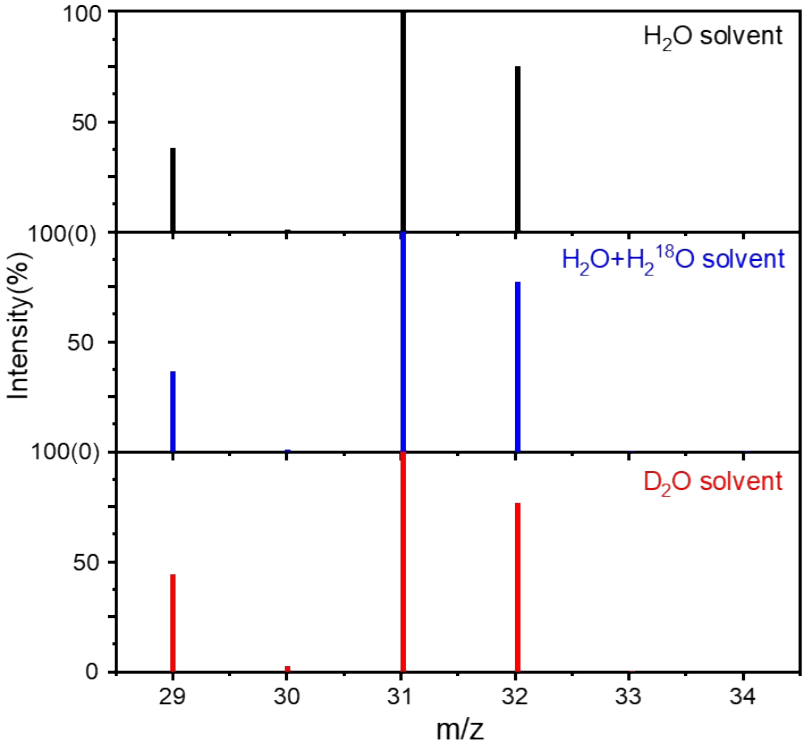

Fig. S14 The GC/Q-TOF-MS spectra from CH_4 oxidation using H_2O, D_2O or H_2O + $H_2{}^{18}O$ as solvent over UiO-66-H. Test conditions: Pressure (CH_4) = 3 MPa, Catalyst: 10 mg UiO-66-H, 0.25 M H_2O_2 (H_2O, D_2O or H_2O + $H_2{}^{18}O$ solvent), 50 ºC (ramp rate of 2 °C min^{-1}), reaction for 4 h. CH_3OOH and $HOCH_2OOH$ could degrade to CH_3OH at high injection temperature of GC. [2-4]

Table S1 The calculated relative energies of the structures in Fig. S3, the (c-l) are consistent with the sequence number corresponding to the structures of Fig. S3.

The number of •OH*	UiO-66-H (eV)			
1	0.0 (a)	--	--	--
2	0.0 (b)	--	--	--
3	0.00 (c)	0.59 (d)	--	--
4	0.00 (e)	-2.02 (f)	-2.17 (g)	-1.28 (h)
5	0.00 (i)	-0.47 (j)	--	--
6	0.00 (k)	-0.45 (l)	--	--

"*" represents the adsorption state.

Table S2 Self-reaction processes of the different amount •OH species adsorbed on Zr-oxo nodes of UiO-66-H.

•OH* number	Self-reactions	Products
3	$3^{\bullet}OH \rightarrow H_2O^* + {}^{\bullet}OOH^*$	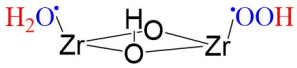
	$3^{\bullet}OH \rightarrow H_2O_2^* + {}^{\bullet}OH^*$	
4	$4^{\bullet}OH \rightarrow H_2O_2^* + 2^{\bullet}OH^*$	
	$4^{\bullet}OH \rightarrow H_2O^* + O_2^* + O_2$	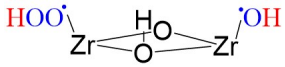
	$4^{\bullet}OH \rightarrow 2H_2O^* + O_2^*$	
	$4^{\bullet}OH \rightarrow {}^{\bullet}OOH^* + {}^{\bullet}OH^* + H_2O$	
5	$5^{\bullet}OH \rightarrow O_2^* + {}^{\bullet}OH^* + 2H_2O$	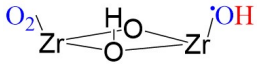
	$5^{\bullet}OH \rightarrow H_2O^* + {}^{\bullet}OOH^* + H_2O_2$	
6	$6^{\bullet}OH \rightarrow 2^{\bullet}OOH^* + 2H_2O^*$	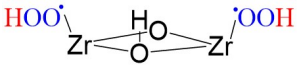
	$6^{\bullet}OH \rightarrow OH^* + {}^{\bullet}OOH^* + H_2O + H_2O_2$	

Table S3 The calculated energy barrier of $^{\bullet}CH_3$ generated on the Zr-oxo nodes adsorbed by $^{\bullet}OH$ or $^{\bullet}OOH$ species over UiO-66-H catalysts. Reactants (R), transition states (TS), products (P).

Added $^{\bullet}OH$	UiO-66-H (eV)				
	R	TS`	TS``	TS`[a]	TS``[a]
$(^{\bullet}OH)_1$/UiO-66-H	0.00	0.89	--	0.87	--
$(^{\bullet}OH)_2$/UiO-66-H	0.00	0.45	--	0.41	--
$(^{\bullet}OH)_3$/UiO-66-H	0.00	1.18	1.03	1.34	1.13
$(^{\bullet}OH)_4$/UiO-66-H	0.00	0.74	--	0.71	0.71
$(^{\bullet}OH)_6$/UiO-66-H	0.00	1.74	1.76	1.69	1.65

[a] H_2O solvation effect

Table S4 Bader charges (|e|) of the selected H, C, O and Zr atoms of the active center in UiO-66-H catalysts with increasing $^{\bullet}OH$ concentration.

Bader charges(|e|)	$(^{\bullet}OH)_1$/UiO-66-H			$(^{\bullet}OH)_2$UiO-66-H			$(^{\bullet}OH)_3$/UiO-66-H		
	R1	TS1	P1	R2	TS2	P2	R3	TS3	P3
H_a	0.60	0.60	0.61	0.59	0.67	0.70	--	--	--
H_b	0.04	0.36	0.66	0.09	0.33	0.58	0.04	0.34	0.66
H_c	0.00	0.05	0.03	0.01	0.06	0.12	0.00	0.08	0.03
H_d	0.03	0.06	0.04	0.03	0.08	0.22	0.05	0.10	0.02
H_e	0.02	0.00	0.06	0.01	0.16	0.08	0.05	0.09	0.09
H_f	--	--	--	--	--	--	0.64	0.61	0.66
C_1	-0.09	-0.17	0.43	-0.15	-0.31	-0.37	-0.15	-0.18	0.40
O_a	-0.98	-1.18	-1.27	-1.18	-1.13	-1.30	-0.67	-0.72	-1.20
O_b	--	--	--	--	--	--	-0.69	-1.01	-1.34
Zr_1	2.78	2.79	2.78	2.79	2.78	2.78	2.78	2.78	2.79
$^{\bullet}O_aH_a$*	-0.38	-0.58	-0.65	-0.59	-0.46	-0.60	--	--	--
$^{\bullet}O_aO_bH_f$*	--	--	--	--	--	--	-0.72	-1.12	-1.88

"*" represents the adsorption state.

Table S5 Bader charges (|e|) of the selected H, C, O and Zr atoms of the active center in UiO-66-H catalysts with increasing •OH concentration.

Bader charges(|e|)	(•OH)$_4$/UiO-66-H			(•OH)$_6$/UiO-66-H		
	R4	TS4	P4	R5	TS6	P5
H_a	0.60	0.66	0.69	--	--	--
H_b	0.08	0.42	0.61	0.07	0.34	0.66
H_c	0.00	0.05	0.01	0.06	0.12	0.06
H_d	0.02	0.07	0.07	0.03	0.12	0.07
H_e	0.01	0.08	0.14	0.01	0.09	0.03
H_f	--	--	--	0.69	0.62	0.62
C_1	-0.12	-0.29	-0.25	-0.17	-0.23	0.38
O_a	-1.20	-1.18	-1.32	-0.35	-0.61	-1.14
O_b	--	--	--	-0.76	-1.00	-1.29
Zr_1	2.78	2.78	2.78	2.77	2.78	2.79
$^{\bullet}O_aH_a$*	-0.60	-0.52	-0.63	--	--	--
$^{\bullet}O_aO_bH_f$*	--	--	--	-0.42	-0.99	-1.81

"*" represents the adsorption state.

Table S6 The predicted reaction rate constant of CH_4 activation on UiO-66-H catalysts with increasing $^{\bullet}OH$ concentration.

$^{\bullet}OH$ Amount	rate constant (s mol L^{-1})
	UiO-66-H
1	6.47×10^{1}
2	3.21×10^{9}
3	1.19×10^{-1}
4	7.11×10^{4}
6	4.91×10^{-4}

Table S7 Performance comparison of UiO-66-H and previously representative catalysts for DSOM reaction using H_2O_2 as an oxidant.

Catalyst	T (°C)	CH_4 (MPa)	H_2O_2 (M)	t h	C1 oxygenates Sel. (%)	C1 oxygenates Yield (μmol g_{cat}^{-1} h^{-1})	Reference
TiO_2	50	3.05	0.5	0.5	0	0	*ACS Catal.*, 2018, **8**, 2567-2576.
TiO_2	light	0.1	hence	3	~60	~90	*Nat. Catal.*, 2018, **1**, 889–896
g-C_3N_4	35	3	0.05	2	-	140	*Int. J. Energy Res.*, 2020, **44**, 2740-2753
Cr_2O_3	50	3	0.5	1	-	260	*Angew. Chem. Int. Ed.*, 2020, **59**, 1216-1219
Fe_2O_3	50	3	0.3	1	77.6	273.6	*Angew. Chem. Int. Ed.*, 2021, **60**, 5811-5815
FeO	50	3	0.3	1	0	0	*Angew. Chem. Int. Ed.*, 2021, **60**, 5811-5815
ZrO_2	70	3	0.5	0.5	0	0	*J. Am. Chem. Soc.*, 2017, **139**, 17694–17699
$0.3Rh_1/ZrO_2$	70	3	0.5	0.5	78	76.7	*J. Am. Chem. Soc.*, 2017, **139**, 17694–17699
$5AuPd/TiO_2$	50	3.05	0.5	0.5	90.3	247.1	*Angew. Chem. Int. Ed.*, 2013, **52**, 1280-1284
2.7 Fe_1N_4/GN	r.t.	2	5	10	94	230	*Chem*, 2018, **4**, 1902-1910
FeO_x/TiO_2	light	0.1	hence	3	~60	~323.6	*Nat. Catal.*, 2018, **1**, 889–896
FeOOH/m-WO_3	light	0.1	hence	4	91	211.2	*Fuel*, 2020, **266**, 117104
FeOOH/$Li_{0.1}WO_3$	light	2	0.1	4	-	~106.5	*Environ. Sci. Technol.*, 2021, **55**, 7711-7720
$0.2Cu_1/C_3N_4$	r.t.	3	4	5	95	166.7	*Chem. Comm.*, 2020, **56**, 14677-14680
2.5Cu/ZSM-5(50)	50	3	0.5	0.5	27	10.4	*ChemPhysChem*, 2017, **19**, 469-478
Pd_1/2DT	light	2	0.1	4	-	46.3	*ACS Catal.*, 2021, **11**, 14038-14046
UiO-66-H	**50**	**3**	**0.25**	**0.5**	**~100**	**364.0**	**This work**

References：

1 V. Wang, N. Xu, J.-C. Liu, G. Tang and W.-T. Geng, *Comput. Phys. Commun.*, 2021, **267**, 108033.

2 Z. Jin, L. Wang, E. Zuidema, K. Mondal, M. Zhang, J. Zhang, C. Wang, X. Meng, H. Yang, C. Mesters and F.-S. Xiao, *Science*, 2020, **367**, 193–197.

3 T. Yu, Z. Li, L. Lin, S. Chu, Y. Su, W. Song, A. Wang, B. M. Weckhuysen and W. Luo, *ACS Catal.*, 2021, **11**, 6684-6691.

4 N. Agarwal, S. J. Freakley, R. U. McVicker, S. M. Althahban, N. Dimitratos, Q. He, D. J. Morgan, R. L. Jenkins, D. J. Willock, S. H. Taylor, C. J. Kiely and G. J. Hutchings, *Science*, 2017, **358**, 223–227.